

The most incompressible metal osmium at static pressures above 750 gigapascals

L. Dubrovinsky^{1*}, N. Dubrovinskaia^{2*}, E. Bykova^{1,2}, M. Bykov², V. Prakapenka³, C. Prescher³, K. Glazyrin⁴, H.-P. Liermann⁴, M. Hanfland⁵, M. Ekholm^{6,7}, Q. Feng^{6,7}, L. V. Pourovskii^{6,8}, M. I. Katsnelson^{9,10}, J. M. Wills¹¹ & I. A. Abrikosov^{7,12}

Metallic osmium (Os) is one of the most exceptional elemental materials, having, at ambient pressure, the highest known density and one of the highest cohesive energies and melting temperatures¹. It is also very incompressible^{2–4}, but its high-pressure behaviour is not well understood because it has been studied^{2–6} so far only at pressures below 75 gigapascals. Here we report powder X-ray diffraction measurements on Os at multi-megabar pressures using both conventional and double-stage diamond anvil cells⁷, with accurate pressure determination ensured by first obtaining self-consistent equations of state of gold, platinum, and tungsten in static experiments up to 500 gigapascals. These measurements allow us to show that Os retains its hexagonal close-packed structure upon compression to over 770 gigapascals. But although its molar volume monotonically decreases with pressure, the unit cell parameter ratio of Os exhibits anomalies at approximately 150 gigapascals and 440 gigapascals. Dynamical mean-field theory calculations suggest that the former anomaly is a signature of the topological change of the Fermi surface for valence electrons. However, the anomaly at 440 gigapascals might be related to an electronic transition associated with pressure-induced interactions between core electrons. The ability to affect the core electrons under static high-pressure experimental conditions, even for incompressible metals such as Os, opens up opportunities to search for new states of matter under extreme compression.

The platinum 5d transition elements Re, Os, and Ir are the densest and stiffest metals^{1,7}. Although a short-lived claim⁴ that Os is stiffer than diamond⁸ was subsequently disproven², there remains scientific interest in the high-pressure behaviour of Os: the bulk modulus values measured by different groups vary substantially (395–435 GPa)^{2,3,5,6,9}, and controversy surrounds reports of a possible pressure-induced isostructural Lifshitz¹⁰ transition (also called an electronic topological transition, ETT) in Os. The ETT arises when distortion of the electronic band structure by an external perturbation results in a topological modification of the Fermi surface.

Os has a hexagonal close-packed (hcp) structure, with two unit cell parameters (*a* and *c*) fully defining the atomic arrangement at a given pressure. The observation³ of an anomaly in the compressibility and pressure dependence of the *c/a* ratio around 25 GPa was attributed to an ETT, but subsequent experimental studies^{2,5,6} at pressures to about 60 GPa failed to detect anomalies and found^{6,11} instead that texturing or non-hydrostatic conditions can greatly complicate the interpretation of X-ray diffraction data; indeed, experimental artefacts may mimic isostructural transitions. Theoretical studies of Os have so far also resulted in an inconsistent picture of its high-pressure beha-

viour. Reports of possible single or multiple anomalies in *c/a* ratio at pressures ranging from 9 GPa to over 25 GPa have been both attributed³ and not attributed¹² to ETT; one study¹³ found evidence for multiple ETTs at pressures up to 130 GPa that did not affect the compressional behaviour of Os, and a further study¹⁴ concluded that there are no peculiarities in the pressure-driven evolution of the atomic and electronic structure of Os. The inconsistencies in the theoretical high-pressure behaviour of Os mirror the difficulties encountered when probing the high-pressure behaviour of 3d hcp metals such as Zn and ε-Fe (refs 15–19). These difficulties add further interest to detailed studies of the 5d element Os, to allow a broader comparison of the crystal chemistry of hcp metals.

Although Os has been experimentally studied^{3,4,6} at pressures up to about 75 GPa, this pressure range is far too narrow to explore the behaviour of one of the most incompressible metals. Data collected at multi-megabar pressures are highly desired, and can be obtained using the double-stage diamond anvil cell (dsDAC) technique⁷, which generates the required ultra-high static pressures. Under such conditions, pressure determination is based on the equation of state (EOS) of one or several standards mixed with the sample being studied (see Methods). The absolute accuracy of the EOS measurements—which is particularly important when aiming to compare experiment against theory—cannot be higher than the accuracy of the static pressure scale. Shock-wave and ramp compression experiments^{20,21} achieve terapascal pressures, but only at high temperatures. The EOSs obtained in experiments below 100 GPa, using different dynamic and static methods and for different standards, tend to agree to within 2–3 GPa, but discrepancies increase with pressure and frequently reach unacceptable levels of the order of tens of gigapascals at a pressure around 0.5 TPa (Fig. 1, Extended Data Fig. 1, examples in ref. 22). Much more accurate results are obtained when using standards with internally consistent EOSs, especially if the materials used as pressure markers have different (or, even better, contrasting) elastic properties^{22–24}, as do gold, platinum, and tungsten.

We conducted experiments in conventional and dsDAs on Au–Pt mixtures at pressures up to 500 GPa, and on Au–W and Pt–W mixtures up to approximately 200 GPa (Fig. 1, Extended Data Figs 1, 2). With Au as the pressure marker²⁰, we fitted the pressure–volume (*P*–*V*) data of Pt using the third-order Birch–Murnaghan (Fig. 1) and the Vinet EOSs (Extended Data Table 1). Both EOSs provide equally good fits, yielding parameters for Pt very close to those obtained from shock-wave data²⁰ (Fig. 1, Extended Data Table 1). Pt and Au were used as pressure markers in two independent powder X-ray diffraction experiments to study the EOS of tungsten (Extended

¹Bavarian Research Institute of Experimental Geochemistry and Geophysics, University of Bayreuth, D-95440 Bayreuth, Germany. ²Laboratory of Crystallography, University of Bayreuth, D-95440 Bayreuth, Germany. ³Center for Advanced Radiation Sources, University of Chicago, Illinois 60437 Argonne, USA. ⁴Photon Sciences, Deutsches Elektronen-Synchrotron (DESY), D-22603 Hamburg, Germany. ⁵European Synchrotron Radiation Facility, BP 220, Grenoble F-38043, France. ⁶Swedish e-Science Research Centre (SeRC), Linköping University, SE-58183 Linköping, Sweden. ⁷Department of Physics, Chemistry and Biology (IFM), Linköping University, SE-58183 Linköping, Sweden. ⁸Centre de Physique Théorique, CNRS, Ecole Polytechnique, 91128 Palaiseau, France. ⁹Radboud University, Institute for Molecules and Materials, Heyendaalseweg 135, 6525AJ Nijmegen, The Netherlands. ¹⁰Department of Theoretical Physics and Applied Mathematics, Ural Federal University, Mira street 19, Ekaterinburg, 620002, Russia. ¹¹Theoretical Division, Los Alamos National Laboratory, Los Alamos, New Mexico 87545 USA. ¹²Materials Modeling and Development Laboratory, National University of Science and Technology ‘MISiS’, 119049 Moscow, Russia.

*These authors contributed equally to this work.

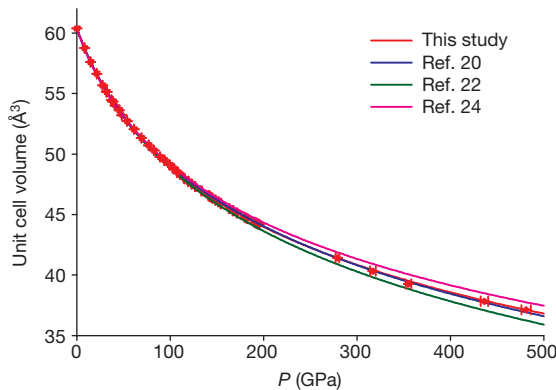


Figure 1 | The dependence of the unit cell volume of Pt on pressure P .

Experimental data points (different symbols correspond to different runs, Au was used as a pressure marker in all experiments, error bars show standard deviations) were fitted using the third-order Birch–Murnaghan EOS (red line, volume at ambient temperature and pressure $V_0 = 60.389(3)$ Å³ per unit cell, EOS parameters $K_{300} = 274(2)$ GPa, $K' = 5.23(3)$). The blue, green, and pink lines are from refs 20, 22, and 24, respectively.

Data Figs 1, 2 and Extended Data Table 1). These experiments yield P - V data that are in remarkable agreement with each other and provide an accurate EOS of W for pressures up to 200 GPa (Extended Data Fig. 1 and Extended Data Table 1). Our data are in close agreement with the EOS of W obtained using a thermodynamic assessment²³, but disagree with extrapolations of the EOSs above about 100 GPa derived from experiments below 1 Mbar (Extended Data Fig. 1). These results confirm the necessity of EOS calibration well above 100 GPa for ultra-high-pressure studies and provide (Extended Data Table 1) a self-consistent set of EOSs for Au, Pt, and W that we use in our experiments with Os.

We studied the compressional behaviour of Os using powder X-ray diffraction experiments in conventional DACs at pressures up to about 200 GPa that were conducted in Ne (Au and W pressure markers, Extended Data Fig. 2) or He (Pt pressure marker). Similar experiments in a dsDAC reached a pressure of 774(10) GPa (according to the Os EOS; see below), where the number in parentheses is one standard deviation; Os adopted the hcp structure even at this pressure (Fig. 2). The only successful experiments in dsDACs with a pressure marker were using the Os–W mixture (Fig. 2), where we achieved a pressure slightly above 500 GPa. The data collected in different runs are consistent (Fig. 3), and the dependence of the unit cell volume on pressure does not show any obvious anomaly and is well described by the third-order Birch–Murnaghan (Fig. 3a) or Vinet EOSs (Extended Data Table 1). The bulk modulus (399(6) GPa fitted with the third-order Birch–Murnaghan EOS) is in agreement with the results of refs 2 (Fig. 3a) and 3 (Extended Data Fig. 3). We do, however, observe two anomalies at approximately 150 GPa and 440 GPa in the ratio of the lattice parameters, c/a , when compressing Os (Fig. 3b). Although these are at the detection limit of our experimental set-up, the anomaly at about 150 GPa was reproduced in three independent runs, and the one above 400 GPa in two runs. Fitting of the P - V data by the third-order Birch–Murnaghan EOS within three pressure ranges—below 120 GPa, between 170 GPa and 400 GPa, and above 400 GPa—gives an interesting result: although fitting over the first and second pressure ranges produces similar EOS parameters ($K_{300} = 397(3)$ GPa, $K' = 4.07(4)$ and $K_{300} = 416(5)$ GPa, $K' = 3.8(1)$, respectively, where the subscript indicates room temperature and the prime denotes differentiation with respect to pressure), we obtain different parameters at pressures above 400 GPa ($K_{300} = 293(5)$ GPa, $K' = 5.4(1)$). These experimentally observed peculiarities are not artefacts and require an explanation: substantial changes of compressibility with pressure are quite

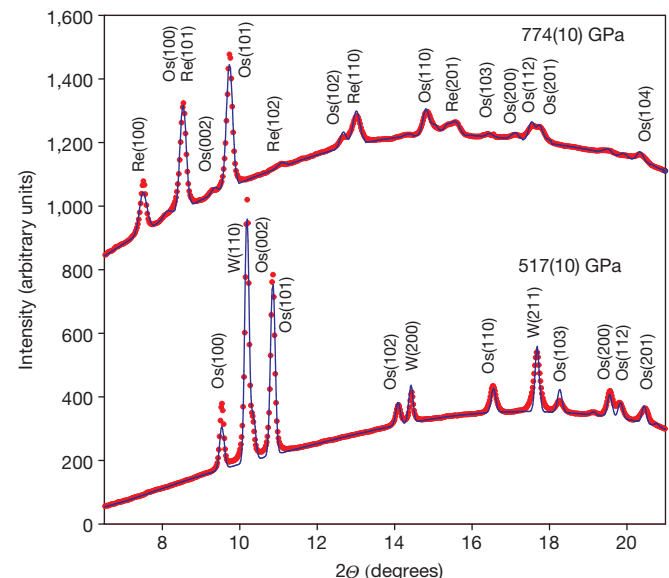


Figure 2 | Diffraction patterns of the samples compressed in dsDACs.

Lower curve, mixture of Os ($a = 2.3232(3)$ Å, $c = 3.7099(11)$ Å) and W ($a = 2.6649(2)$ Å, pressure marker); X-ray wavelength of 0.3344 Å. Upper curve, Os ($a = 2.2488(2)$ Å, $c = 3.555(2)$ Å, pressure determined from our Os EOS); X-ray wavelength of 0.2898 Å. Reflections of highly textured Re at approximately 110 GPa are due to the Re support of the secondary anvil. Experimental data are shown by red dots; continuous blue curves are simulations using the full-profile (GSAS) software. Θ is the diffraction angle; the labels on the peaks indicate the Miller indices of the corresponding diffraction reflection of the given metal; diffraction lines of secondary anvils are not visible; the pressures given above the curves designate at which pressure in a dsDAC the diffraction patterns were collected.

common for materials undergoing pressure-induced spin crossover¹⁹, but are not expected for heavy 5d elements such as Os.

The behaviour of the c/a ratio of Os suggests that an ETT is the most likely explanation for the observed peculiarities¹⁹. In first-principles electronic structure calculations for Os at different compressions in the framework of dynamical mean-field theory²⁵ (see Methods), we observe two ETTs at Γ and L points of the hcp Brillouin zone at pressures of approximately 100 GPa and 180 GPa, respectively (Extended Data Figs 4, 5). This result agrees with the pressure range in which the first c/a ratio anomaly appears experimentally (Fig. 3b). The behaviour of the bands at Γ and L points for increasing pressure is remarkably similar to that observed recently in the isoelectronic hcp Fe (ref. 19). We observe a rather strong influence of many-electron effects beyond the local density approximation within density functional theory (DFT) on the band structure at Γ and L points even though Os can be classified as a weakly correlated metal (Extended Data Fig. 4). The inclusion of correlations between 5d electrons moves the ETTs at these high symmetry points to higher pressure (Extended Data Fig. 5), improving the agreement with experiment. However, increasing the pressure further does not lead to any new ETTs up to a pressure $P = 477$ GPa (Extended Data Fig. 6), even when including the spin-orbit interaction (Methods and Extended Data Figs 7, 8). Consequently, the origin of the second anomaly in the c/a ratio seen in Fig. 3b remains unknown.

In solid metals, the outermost (valence) electrons are no longer associated with their respective atoms and instead form electronic bands that bond the atoms together. Because the inner-core electrons remain tightly bound to their nuclei and do not contribute to the bonds, they are often considered irrelevant when determining the properties of the material. But compression increases the overlap between the electronic clouds, as seen in the plot of the electronic density of states (DOS) of Os in Fig. 4, where the low-lying localized 5p and 4f states start to interact with each other at $P = 392$ GPa. This

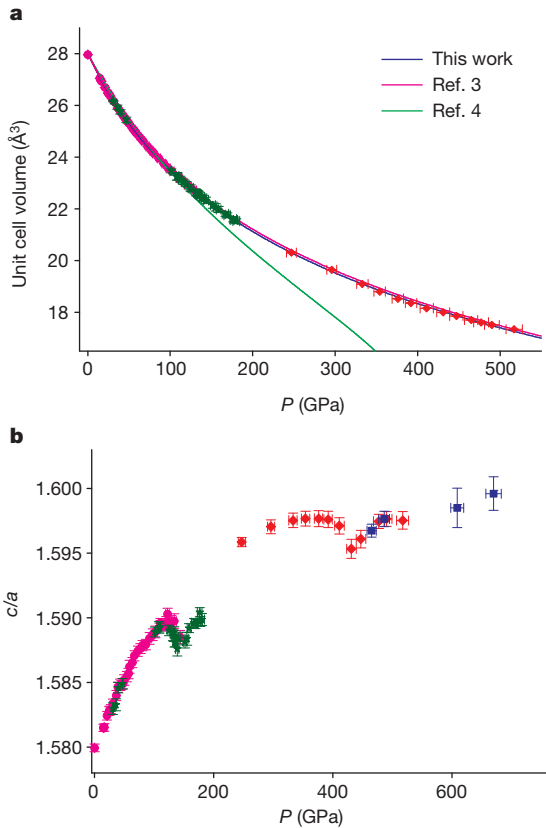


Figure 3 | Experimental dependence of the unit cell volume and the ratio of the lattice parameters c/a of Os on pressure P . **a, b,** Different symbols correspond to different pressure markers in different runs (solid magenta dots, Au and W pressure markers; green stars, Pt marker; red diamonds, W pressure marker; blue square, Os itself; error bars show standard deviations). Experimental data points were fitted using the third-order Birch–Murnaghan EOS (blue line, $V_0 = 28.02(4)$ Å³ per unit cell, $K_{300} = 399(6)$ GPa, $K' = 4.04(4)$). The magenta and green lines are from refs 3 and 4, respectively.

pressure for the core-level crossing (CLC) transition is in good agreement with the pressure at which we see the c/a ratio anomaly in our experiments, suggesting that interactions between $5p$ and $4f$ states might cause the observed peculiarity.

The effect of the CLC transition on thermodynamic properties must be indirect. Using the pseudopotential transformation²⁶, one can establish a relation between the smooth part of the valence orbitals ψ_i^v , which determine the bonding, and the core orbitals ψ_j^c . The former are solutions of the Schrödinger-like equation

$$\left[-\frac{\hbar^2}{2m} \nabla^2 + \hat{V} \right] \tilde{\psi}_i^v(\mathbf{r}) = \varepsilon_i^v \tilde{\psi}_i^v(\mathbf{r}) \quad (1)$$

where \hbar is the reduced Planck constant, m is the mass of the electron, \mathbf{r} is the position vector, ε_i^v are the eigenvalues of the orbitals, and $\hat{V} = V + \hat{V}^R$ is the pseudopotential, with V an effective potential that acts on the electron. The non-local operator \hat{V}^R acts upon $\tilde{\psi}_i^v$ according to

$$\hat{V}^R \tilde{\psi}_i^v(\mathbf{r}) = \sum_j \left(\varepsilon_i^v - \varepsilon_j^c \right) \langle \psi_j^c | \tilde{\psi}_i^v \rangle \psi_j^c(\mathbf{r}) \quad (2)$$

Well-separated and atomic-like core states are often considered ‘frozen’, with no pressure-dependent influence on the valence states; this explains the success of modern pseudopotential approaches when studying matter under extreme conditions. But substantial reconstruction of inner $5p$ and $4f$ states can affect chemical bonding and thereby structural properties of solids via modification of the non-local operator \hat{V}^R in equation (2).

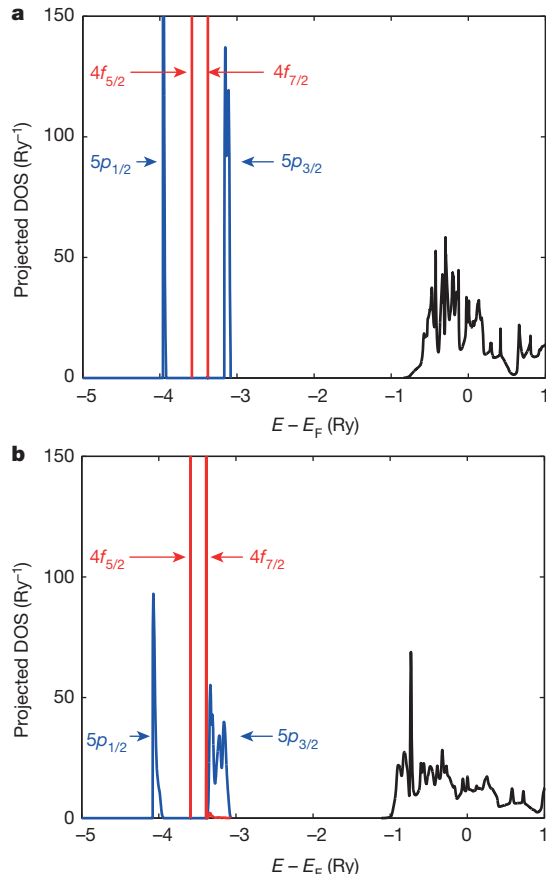


Figure 4 | Calculated electronic density of states (DOS) of Os as a function of energy E (relative to the Fermi energy E_F). **a, b,** DOS at pressures of 0 GPa (a) and 392 GPa (b). Experimental lattice parameters were used in the calculations. $6s$, $6p$, $5d$, and $5f$ electrons form well-defined bands near the Fermi energy at all the pressures examined in this study. $5p$ electrons occupy $5p_{1/2}$ and $5p_{3/2}$ states, which are split owing to spin–orbit interaction; $4f$ electrons occupy $4f_{5/2}$ and $4f_{7/2}$ states. They behave as core electrons forming fully localized states at $P = 0$ GPa. However, at $P = 392$ GPa, the $5p$ states are broadened. Importantly, one clearly sees in b that $5p_{3/2}$ and $4f_{7/2}$ states start to interact with each other, and the CLC transition takes place. This interaction might be responsible for the peculiarity observed in our experiments at ultra-high pressure.

Even in the simplest model of polarized ionic cores of small radius, where the pseudopotential reduces to a local operator, its Fourier component $v_{ps}(q)$ is²⁷

$$v_{ps}(q) = Z v_C(q) - \sum_k \int_{-\infty}^{\infty} \frac{d\omega}{2\pi} \frac{\alpha(i\omega)}{\left(1 + \omega_p^2/\omega^2\right)^2} v_C(k) \times v_C(|\mathbf{k} - \mathbf{q}|) \frac{\mathbf{k}(\mathbf{k} - \mathbf{q})}{-i\omega + \varepsilon_{\mathbf{k}-\mathbf{q}}} \quad (3)$$

where Z is the ionic charge, \mathbf{q} is the wave vector of the Fourier component of the pseudopotential, $v_C(q) = 4\pi e^2/q^2$ is the Fourier component of the Coulomb interaction, \mathbf{k} is the electron wave vector, $\varepsilon_{\mathbf{k}}$ is the dispersion relation for the conduction electrons, ω_p is their plasma frequency, and $\alpha(i\omega)$ is the ion core polarizability at imaginary frequencies. In this model, reconstruction of the inner states affects the electron–ion interaction via the function $\alpha(i\omega)$; Os under ultra-high pressure seems to provide the first real example of this kind of effect. In a sense this effect resembles the well-known phenomenon of atomic collapse²⁸, where, as one moves across the periodic table, f electron states move from their outer effective potential well to the inner well (which explains the existence of rare-earth and actinide groups).

Although the effects we document are much weaker, the unavoidable strong mixing of $4f$ and $5p$ states at the CLC changes atomic polarizability and therefore the potential of the ion–electron interaction. Figure 4b shows that the overlap of $5p$ states increases with pressure, which equates to an increase of their effective radius. This should make their contribution to the ionic polarizability larger, and translate the effect of the CLC—a transition that is expected to be common, at least for the transition metals of the sixth period—to the valence electrons.

Relating electronic transitions to lattice parameter anomalies is generally nontrivial (Methods). For instance, a conventional ETT caused by a Fermi surface topology change need not result in a visible anomaly in the pressure dependence of lattice parameters at temperature $T = 0$ (Extended Data Figs 9, 10, Extended Data Table 1) because the ETT gives rise to a pronounced anomaly in the third derivative of the thermodynamic potential and induces some kinks in the second derivative (this is the reason it is often called “the second-and-a-half”-order transition¹⁰). But the ETT gives rise to a divergence in the thermal expansion, resulting in an observable anomaly in the c/a ratio at finite temperatures (Methods). A similar situation may exist regarding the new type of electronic transition observed in our experiments at ultrahigh pressure, even though the effect of the crossing of deep $4f$ and $5p$ levels should be weaker than the effect arising from the Fermi surface topology modification; the experimentally observed anomaly in the c/a ratio at approximately 440 GPa is weaker than the one at approximately 150 GPa (Fig. 3b).

Our findings demonstrate that extreme compression can change the nature of core electrons. This effect has been examined in static high-pressure experiments for soft simple metals like Li (ref. 29) and Na (ref. 30), but recent ramp compression experiments on diamond²¹ have indicated that qualitatively new static pressure levels are needed to affect the core electrons of less compressible transition metals or covalently bonded materials. By compressing Os, one of most incompressible metals, to over 770 GPa, we were able to access this regime and observe a new type of electronic transition, the CLC transition, that involves pressure-induced interactions between core electrons, and leads to observable changes of the material properties. We believe that the ability to reach sufficiently high pressure levels to affect the core electrons of transition metals in static high-pressure experiments will open up opportunities in the search for new states of matter.

Online Content Methods, along with any additional Extended Data display items and Source Data, are available in the online version of the paper; references unique to these sections appear only in the online paper.

Received 20 January; accepted 17 June 2015.

Published online 24 August 2015.

- Young, D. A. *Phase Diagrams of the Elements* (Univ. of California Press, 1991).
- Kenichi, T. Bulk modulus of osmium: high-pressure powder x-ray diffraction experiments under quasihydrostatic conditions. *Phys. Rev. B* **70**, 012101 (2004).
- Occelli, F. et al. Experimental evidence for a high-pressure isostructural phase transition in osmium. *Phys. Rev. Lett.* **93**, 095502 (2004).
- Cynn, H., Klepeis, J. E., Yoo, C.-S. & Young, D. A. Osmium has the lowest experimentally determined compressibility. *Phys. Rev. Lett.* **88**, 135701 (2002).
- Armentrout, M. M. & Kavner, A. Incompressibility of osmium metal at ultrahigh pressures and temperatures. *J. Appl. Phys.* **107**, 093528 (2010).
- Godwal, B. K., Yan, J., Clark, S. M. & Jeanloz, R. High-pressure behavior of osmium: an analog for iron in Earth's core. *J. Appl. Phys.* **111**, 112608 (2012).
- Dubrovinsky, L., Dubrovinskaia, N., Prakapenka, V. & Abakumov, A. Implementation of micro-ball nanodiamond anvils for high-pressure studies above 6 Mbar. *Nature Commun.* **3**, 1163 (2012).
- Occelli, F., Loubeire, P. & Letoullac, R. Properties of diamond under hydrostatic pressures up to 140 GPa. *Nature Mater.* **2**, 151–154 (2003).
- Voronin, G. A., Pantea, C., Zerda, T. W., Wang, L. & Zhao, Y. Thermal equation-of-state of osmium: a synchrotron X-ray diffraction study. *J. Phys. Chem. Solids* **66**, 706–710 (2005).

- Lifshitz, I. M. *Zh. Eksp. Teor. Fiz.* **38**, 1569 (1960); Anomalies of electron characteristics of a metal in the high-pressure region. *Sov. Phys. JETP* **11**, 1130 (1960).
- Weinberger, M. B., Tolbert, S. H. & Kavner, A. Osmium metal studied under high pressure and nonhydrostatic stress. *Phys. Rev. Lett.* **100**, 045506 (2008).
- Ma, Y. M. et al. Electronic and crystal structures of osmium under high pressure. *Phys. Rev. B* **72**, 174103 (2005).
- Koudela, D., Richter, M., Möbius, A., Koepernik, K. & Eschrig, H. Lifshitz transitions and elastic properties of osmium under pressure. *Phys. Rev. B* **74**, 214103 (2006).
- Liang, Y. & Fang, Z. First-principles study of osmium under high pressure. *J. Phys. Condens. Matter* **18**, 8749–8759 (2006).
- Kenichi, T. Structural study of Zn and Cd to ultrahigh pressures. *Phys. Rev. B* **56**, 5170–5179 (1997).
- Kenichi, T. Absence of the c/a anomaly in Zn under high pressure with a helium-pressure medium. *Phys. Rev. B* **60**, 6171–6174 (1999).
- Klotz, S., Braden, M. & Besson, J. M. Is there an electronic topological transition in zinc under high pressure? *Phys. Rev. Lett.* **81**, 1239–1242 (1998).
- Steinle-Neumann, G., Stixrude, L. & Cohen, R. Absence of lattice strain anomalies at the electronic topological transition in zinc at high pressure. *Phys. Rev. B* **63**, 054103 (2001).
- Glazyrin, K. et al. Importance of correlation effects in hcp iron revealed by a pressure-induced electronic topological transition. *Phys. Rev. Lett.* **110**, 117206 (2013).
- Yokoo, M. et al. Ultrahigh-pressure scales for gold and platinum at pressures up to 550 GPa. *Phys. Rev. B* **80**, 104114 (2009).
- Smith, R. F. et al. Ramp compression of diamond to five terapascals. *Nature* **511**, 330–333 (2014).
- Dorogokupets, P. I. & Dewaele, A. Equations of state of MgO, Au, Pt, NaCl-B1, and NaCl-B2: internally consistent high-temperature pressure scales. *High Press. Res.* **27**, 431–446 (2007).
- Sokolova, T. S., Dorogokupets, P. I. & Litasov, K. D. Self-consistent pressure scales based on the equations of state for ruby, diamond, MgO, B2–NaCl, as well as Au, Pt, and other metals to 4 Mbar and 3000 K. *Russ. Geol. Geophys.* **54**, 181–199 (2013).
- Holmes, N. C., Moriarty, J. A., Gather, G. R. & Nellis, W. J. The equation of state of platinum to 660 GPa. *J. Appl. Phys.* **66**, 2962–2967 (1989).
- Kotliar, G. et al. Electronic structure calculations with dynamical mean-field theory. *Rev. Mod. Phys.* **78**, 865–951 (2006).
- Martin, R. M. *Electronic Structure: Basic Theory and Practical Methods* 210 (Cambridge Univ. Press, 2004).
- Katsnelson, M. I. & Trefilov, A. V. The effect of van der Waals and Born-Mayer interactions of ionic cores on the atomic properties of the alkali metals. *Fiz. Tverdogo Tela* **30**, 3299–3310 (1988).
- Karazija, R. I. The collapse of the excited electron orbit and the peculiarities of the atomic spectra. *Usp. Fiz. Nauk* **135**, 79–115 (1981).
- Matsuoka, T. & Shimizu, K. Direct observation of a pressure-induced metal-to-semiconductor transition in lithium. *Nature* **458**, 186–189 (2009).
- Ma, Y. et al. Transparent dense sodium. *Nature* **458**, 182–185 (2009).

Acknowledgements L.D. and N.D. acknowledge financial support from the Deutsche Forschungsgemeinschaft (DFG) and the Federal Ministry of Education and Research (BMBF), Germany. N.D. thanks the DFG for funding through the Heisenberg Program and the DFG project number DU 954-8/1, and the BMBF for grant number 5K13WC3 (Verbundprojekt 05K2013, Teilprojekt 2, PT-DESY). M.E., Q.F., and I.A.A. acknowledge support from the Swedish Foundation for Strategic Research programme SRL grant numbers 10-0026, the Swedish Research Council (VR) grant numbers 621-2011-4426, the Swedish Government Strategic Research Area Grant Swedish e-Science Research Centre (SeRC), and in Materials Science “Advanced Functional Materials” (AFM). The work was supported by the Ministry of Education and Science of the Russian Federation (grant number 14.Y26.31.0005). The simulations were carried out using supercomputer resources provided by the Swedish national infrastructure for computing (SNIC). M.I.K. acknowledges financial support from the ERC Advanced grant number 338957 FEMTO/NANO and from NWO via a Spinoza Prize. Portions of this work were performed at GeoSoilEnviroCARS (Sector 13), Advanced Photon Source (APS), Argonne National Laboratory. GeoSoilEnviroCARS is supported by the National Science Foundation – Earth Sciences (EAR-1128799) and Department of Energy - GeoSciences (DE-FG02-94ER14466). This research used resources of the Advanced Photon Source, a US Department of Energy (DOE) Office of Science User Facility operated for the DOE Office of Science by Argonne National Laboratory under contract number DE-AC02-06CH11357.

Author Contributions L.D., N.D., E.B., M.B., V.P., C.P., K.G., H.-P.L., and M. H. conducted the experiments. L.D. and N.D. processed the experimental data. M.E., Q.F., L.V.P., M.I.K., J.M.W., and I.A.A. performed the theoretical analysis. The manuscript was written by L.D. and I.A.A. with contributions from all other authors. All the authors commented on drafts and have approved the final version of the manuscript.

Author Information Reprints and permissions information is available at www.nature.com/reprints. The authors declare no competing financial interests. Readers are welcome to comment on the online version of the paper. Correspondence and requests for materials should be addressed to L.D. (Leonid.Dubrovinsky@uni-bayreuth.de) or I.A.A. (Igor.Abrikosov@ifm.liu.se).

METHODS

Materials. Au (99.999% purity, 1-μm particle size), Pt (99.999% purity, 2-μm particle size), W (99.999% purity, 1-μm particle size), and Os (99.99% purity, 1-μm particle size) powders were purchased from Goodfellow Inc.

Diamond anvil cell experiments. For all our experiments we used piston-cylinder BX90 type DACs with a large optical aperture produced at BGI. Diamonds with culet sizes of 250 μm or 300 μm were used in conventional DAC experiments below 70 GPa or as primary anvils in double-stage DACs. Compression of Au, Pt, W, and Os powders in a He or Ne pressure medium above 100 GPa was conducted with bevelled diamonds with 120-μm cutlets. The secondary anvils were produced by direct conversion of glassy carbon balls with diameters of 10–20 μm. Re or Ir were used as gasket materials. Gaskets were indented to a thickness of 20–35 μm in different experiments and holes with diameters of 125–150 μm were drilled into the centre of the indentation. As a pressure transmitting medium, He and Ne was loaded at pressures of 1.2–1.4 kbar; in some experiments with double-stage DACs, liquid paraffin wax was used. Cavities in diamond anvils for experiments with double-stage DACs were made by a picosecond pulsed laser.

X-ray diffraction measurements. We conducted *in situ* X-ray high-pressure experiments at the Bayerisches Geoinstitut (Germany), at ID09 at ESRF (France), at ECB at PETRA III (Germany), and at 13-IDD at Advanced Photon Source, APS (USA). At the Bayerisches Geoinstitut, we obtained powder X-ray diffraction data with a system consisting of a Rigaku FRD high-brilliance generator (90 kW) and APEX CCD Area Detector. The MoK_α radiation (tube voltage 60 kV, tube current 55 mA, cathode gun $0.1 \times 0.1 \text{ mm}^2$) was focused with MaxFlux X-ray optics and further collimated down to a FWHM beam size of about 30 μm. At the ID09 at ESRF, the data were collected with the MAR555 detector using an X-ray beam with a wavelength of approximately 0.41 Å and a beam size down to $5 \times 5 \text{ } \mu\text{m}^2$. At the ECB at PETRA III, the data were collected with the Perkin Elmer detector using an X-ray beam with a wavelength of approximately 0.29 Å and a beam size as small as $1.5 \times 1.5 \text{ } \mu\text{m}^2$. At the 13-IDD station (GSECARS), we used a MAR-165 CCD area detector and a highly focused beam (about $3 \times 4 \text{ } \mu\text{m}^2$) with a wavelength of 0.3344 Å. The collected images were integrated using the Fit2D or GADDS programs to obtain a conventional diffraction pattern. Data analysis was conducted using the GSAS package.

Computational details. To include electronic correlation effects for the partially-filled Os 5d band beyond the standard DFT framework we used an local density approximation + dynamical mean-field theory (LDA+DMFT) approach^{25,31}. This approach is based on a full-potential linear augmented plane-wave + local orbitals technique as implemented in the Wien2k code⁴⁰ in conjunction with the DMFT implementation provided by the TRIQS package^{31–34}. Our LDA+DMFT framework is fully self-consistent in the charge density. The LDA+DMFT calculations were performed within the scalar-relativistic approximation and using a k -mesh with $32 \times 32 \times 32$ points in the full Brillouin zone. The spin-orbit coupling was not included because LDA calculations show that it has a negligible effect on the electronic structure in the vicinity of the Fermi level. The DMFT quantum impurity problem was solved using the numerically-exact imaginary-time hybridization-expansion continuous-time quantum Monte Carlo (CT-QMC) method³⁵. A large number of Monte Carlo cycles, more than 512 million, were performed to obtain a well converged DMFT local self-energy. We adopted a stochastic version of the maximum entropy method³⁶ for the analytical continuation of the CT-QMC self-energy to the real frequency axis. For the Coulomb interaction strength U and Hund's coupling constant J we used the values $U = 2.8 \text{ eV}$ and $J = 0.55 \text{ eV}$ that are estimated in ref. 37. The qualitative results of our LDA+DMFT calculations are not very sensitive to the exact values of U and J . We used the ‘around mean-field form’³⁸ for the double counting correction, which is suitable for weakly correlated metallic systems.

In calculations of band structure at the level of DFT³⁹ within the LDA or semi-local generalized gradient approximation (GGA), we used two complementary methods, the full potential (linear) augmented plane waves + local orbitals method as implemented in the Wien2k code⁴⁰ and the electronic-structure method⁴¹ RSPT. Both are all-electron methods, which do not impose any approximations on the shape of the one-electron potential, and they are known to generate very similar results. The former method allows us to directly compare the LDA and LDA+DMFT results. These methods are particularly suited to high-pressure calculations because the basis functions for any energy, including nominally deep core states, can be treated as ‘valence’ states.

For calculations with the Wien2k code, we used a k -mesh consisting of $32 \times 32 \times 32$ k -points in the full Brillouin zone. The size of the plane-wave basis set is given by the cutoff parameter K_{\max} . In our calculations, we kept the product between K_{\max} and the radius of the real-space muffin-tin spheres to $K_{\max} \times R_{\text{MT}} = 10$. At pressures of 0 GPa, 134 GPa, 247 GPa, and 477 GPa, we set $R_{\text{MT}} = 2.5$ atomic units (a.u.), 2.34 a.u., 2.27 a.u., and 2.16 a.u., respectively.

Wien2k LDA results give the most direct comparison to our LDA+DMFT results, because same computational scheme at the LDA level is used.

To calculate the band-projected density of states (DOS) we used RSPT⁴¹. RSPT is an all-electron, full-potential electronic structure method that uses a basis of site-centred spherical waves (a generalization of augmented muffin-tin orbitals) in the self-consistent Kohn–Sham formalism⁴⁰ to calculate the electron density and total energy. We used LDA, as well as two gradient corrected functionals, AM05^{42,43} and PBE⁴⁴—well-known examples of the accuracy DFT can achieve⁴⁵. We used RSPT to predict the electron DOS of Os in the hexagonal close-packed (hcp) structure at pressures up to about 700 GPa. At these pressures, we find that a basis corresponding to 4f, 5s, 5p, 5d, 5f, 6s, and 6p atomic states is sufficiently complete; adding 4d functions to the valence yields negligible changes in the calculated DOS. Bases are scalar-relativistic: the spin–orbit interaction is included variationally.

Calculations of band structure and DOS were carried out at the experimental values of the lattice parameters for each value of pressure. For a few lattice parameters, the calculations were carried out using both the Wien2k code with LDA, and the RSPT code with GGA-PBE; the obtained DOS are very similar. The electronic structure calculated for a fixed lattice parameter is known to be quite insensitive to the use of LDA or GGA in the calculations⁴⁶. When calculating the c/a ratio using RSPT, enthalpy was optimized at fixed pressure on a grid of pressures. Using Wien2k, energy was minimized at fixed volume.

Influence of correlation effects. To underline the importance of correlation effects in calculations of the electronic structure of Os, we compare the results of LDA+DMFT and LDA calculations in Extended Data Figs 4 and 5. The difference is quite noticeable. In our LDA calculations, we do not observe any ETTs at the Γ point as pressure increases, because at 0 GPa the corresponding band is already well above the Fermi level. This result is in contrast to that of ref. 13, where an ETT was found at this point, but in agreement with ref. 14, in which no ETT was reported. This discrepancy is due to the different values for the lattice constant that were used in the LDA calculations. We used experimental room-temperature values of the lattice parameters. Using the LDA lattice constants from ref. 13, we recover the band energy below the Fermi level at the Γ point. Assuming the GGA lattice constants from ref. 14, we reproduce the results of this work at the Γ point.

Our LDA calculations also predict that the L-point ETT occurs at a much smaller pressure than our LDA+DMFT calculations, around 100 GPa (Extended Data Figs 4 and 5). In ref. 14, this band at the L point was predicted to be just below the Fermi level at 129 GPa; no ETTs are reported in this pressure range. Using the same lattice constants as in ref. 14, we reproduce these results within LDA. We also find that along the L–H line, the band energy is just above the Fermi level, but this part of the Brillouin zone is not shown in ref. 14. Thus, we attribute discrepancies between the LDA- and GGA-based studies to differences in the EOS rather than to the exchange-correlation potential.

The discussion above shows that the electronic structure at the Γ and L points is quite sensitive to volume changes, and that the occurrence, as well as the position of ETTs in the LDA/GGA picture, depends sensitively on the accuracy of the assumed EOS. The accuracy of the calculated EOS in Os depends on the approximation for the electron–electron interactions used in calculations, as is discussed below. In view of this uncertainty, the most reliable description of the electronic structure is obtained using the experimentally measured lattice parameters⁴⁶. We adopted this strategy, and show all the electronic structure plots at the experimental lattice parameters. We did not detect any substantial difference between the electronic structure calculated with the Wien2k code and with RSPT methods.

Influence of relativistic effects. Because Os is a heavy element, the importance of the spin–orbit coupling (SOC) should be investigated. Using LDA, we calculated the band structure in both the scalar-relativistic approximation and with the inclusion of SOC using the Wien2k code⁴⁰; the results are shown in Extended Data Figs 7 and 8. Some of the bands are split as a result of the inclusion of SOC. However, no new features are seen in the immediate vicinity of the Fermi level. In both cases, we find that one ETT has already taken place at the L point of the hcp Brillouin zone at a pressure of 134 GPa (Extended Data Fig. 7). We do not see any new ETTs upon increasing the pressure to 477 GPa (Extended Data Fig. 8). Instead, we see that the agreement between LDA and LDA+DMFT improves at high pressure, as expected, because the importance of correlation effects decreases with increasing pressure. This observed agreement indicates the internal consistency of our calculations.

Calculated equation of state. The calculations of the EOS and the lattice parameters using the LDA+DMFT approach are very time consuming, and their numerical accuracy is insufficient to distinguish weak peculiarities of the lattice parameters, such as the c/a ratio⁴⁷. We therefore focus on the results obtained within the LDA and GGA of the DFT, and compare our results with experiment, as well as with data available in the literature (see Extended Data Fig. 9 and 10 and Extended Data Table 1).

Relationship between electronic transitions and anomalies in lattice parameters. Let us first consider an ETT due to the change of the Fermi surface topology. Although we have shown the importance of many-electron effects for hcp Os, they mainly influence band positions at the Γ and L points, while the metal remains weakly correlated. Thus, we can use the one-electron picture for a qualitative discussion. For three-dimensional systems the main effect of correlations on the ETT is the change of coefficients at the singularities⁴⁸. The character of the anomalies due to the ETT is different at low temperatures (lower than typical phonon energies) and at high ones. The initial anomaly is in the DOS at the Fermi energy, which within the one-electron picture is a square root singularity, for example, $\delta N(E_F) \propto \sqrt{z}\theta(z)$, where z is the distance between the Fermi energy E_F and the Van Hove singularity E_C ($z = E_F - E_C$), and $\theta(z)$ is the Heaviside function¹⁰. In the case of an appearance of a new hole pocket¹⁹ below the critical volume V_{ETT} , the change in the DOS is $\delta N(E_F) \approx (V_{\text{ETT}} - V)^{1/2}$. The anomaly yields a sharp peculiarity in the third derivative of the thermodynamic potential Ω , and induces some kinks in the second derivative. However, it does not necessarily lead to a visible peculiarity of the pressure dependence of the lattice parameters at $T = 0$ K, in agreement with our calculations (Extended Data Fig. 10). Still, in hcp metals the effect of the ETT on the lattice parameters can be detected experimentally at finite temperature, owing to the anisotropy of the thermal expansion coefficients α_c and α_a along the c and a directions of the crystal lattice, respectively.

Indeed, α_c and α_a can be evaluated from the phonon F^{phon} and the electron F^{el} contributions to the free energy of the hcp metal^{49,50}:

$$\begin{aligned} \alpha_a &= \frac{1}{3V(B_{11}B_{22}-B_{12}^2)} \left[-(B_{22}+B_{12}) \frac{\partial^2 F^*}{\partial T \partial \epsilon_y} + (B_{12}+B_{11}) \frac{\partial^2 F^*}{\partial T \partial \epsilon_c} \right] \\ \alpha_c &= \frac{1}{3V(B_{11}B_{22}-B_{12}^2)} \left[-(B_{22}-2B_{12}) \frac{\partial^2 F^*}{\partial T \partial \epsilon_y} + (B_{12}-2B_{11}) \frac{\partial^2 F^*}{\partial T \partial \epsilon_c} \right] \end{aligned} \quad (4)$$

where $F^* = F^{\text{phon}} + F^{\text{el}}$, T is the temperature, V is the volume, $d\epsilon_v \equiv d\ln(V)$, $d\epsilon_c \equiv d\ln(c/a)$, and the coefficients B_{ij} are defined via the hcp elastic constants C_{ij} according to

$$\begin{aligned} B_{11} &= \frac{2}{9} \left(C_{11} + C_{12} + \frac{1}{2} C_{33} + 2C_{13} \right) \\ B_{22} &= \frac{2}{9} \left(C_{11} + C_{12} + 2C_{33} - 4C_{13} \right) \\ B_{12} &= \frac{1}{9} \left(C_{33} + C_{13} - C_{11} - C_{12} \right) \end{aligned}$$

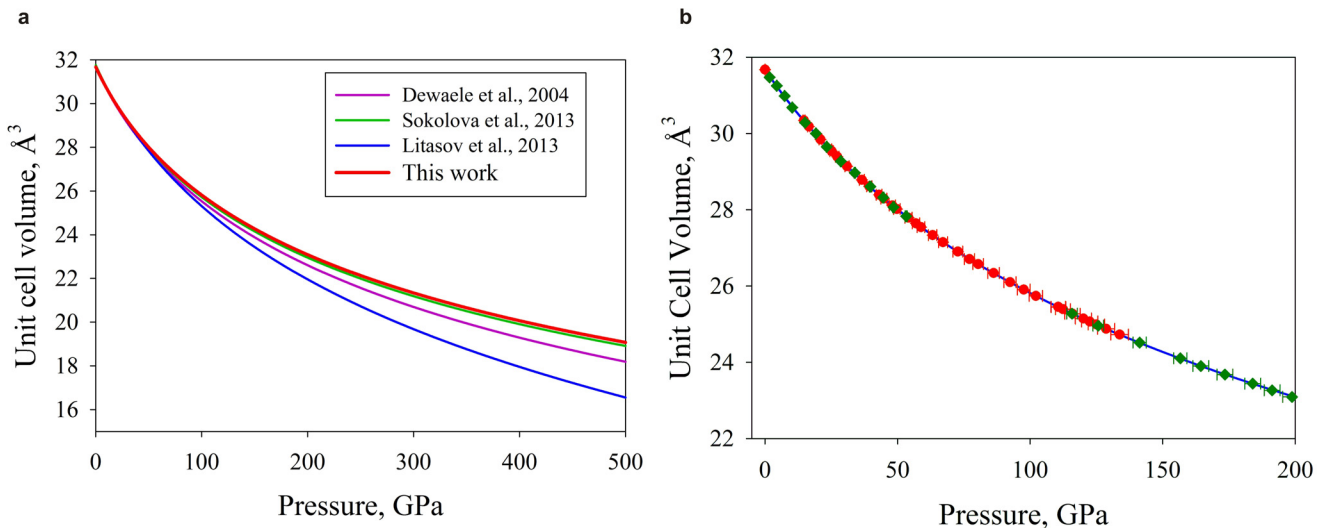
Thus, the anisotropy of the thermal expansion is an inherent property of an hcp metal, but it should become stronger at the point of the ETT. The contribution due to the ETT to the electronic Grüneisen parameter and thus to the electronic thermal expansion coefficient is proportional to $\partial \delta N(E_F) / \partial u \propto 1/\sqrt{z}$ (where u is the dilatation) and is divergent at the point of the ETT. However, this contribution is dominant only at a very low temperatures (typically of the order of 10 K or below), and phonon contribution should be considered. For acoustic phonons with small wave vectors, the Grüneisen parameter and thus the thermal expansion coefficient are proportional to $\partial C_{ii} / \partial u$ (typically there is only one shear modulus that is especially sensitive to the ETT, and it is the modulus that should be considered⁵¹). Because⁵¹ $\partial C_{ii} \propto \delta N(E_F)$, the low-temperature phonon thermal expansion coefficient is as singular as the electronic one. The anomaly in phonon frequencies all over the Brillouin zone, except at the vicinity of the Γ point, is determined by the change of effective interatomic potential via the screening anomaly, which is weaker and proportional to $(-z)^{3/2}\theta(-z)$ (ref. 48); as a result, at high enough temperatures, we expect a square-root singularity in the thermal expansion coefficient.

The temperature at which a crossover occurs from a stronger to a weaker singularity depends on peculiarities of the phonon spectra of a particular material. The peculiarity of the c/a ratio appears in the experiment as an effect that is integrated over the temperature, and therefore the contribution from strong peculiarities at low temperature should remain visible in room-temperature experiments. For example, although for hcp Ti the crossover temperature is about 150 K⁵⁰, the temperature induced change of the c/a ratio between 0 K and room temperature is of the order of 0.5%, judging from the experiment reported⁴⁹. In hcp Fe, the behaviour of the bands at the Γ and L points is very similar to the case of Os and the peculiarity of c/a is also visible¹⁹. The difference between hcp Fe and Os is that in the former metal, the bands cross the Fermi level almost at the same pressure, whereas in the latter, the crossover takes place within a larger pressure range.

A CLC transition discovered in this work may also lead to an observable peculiarity of the c/a ratio. The anisotropy of the thermal expansion in hcp metals is

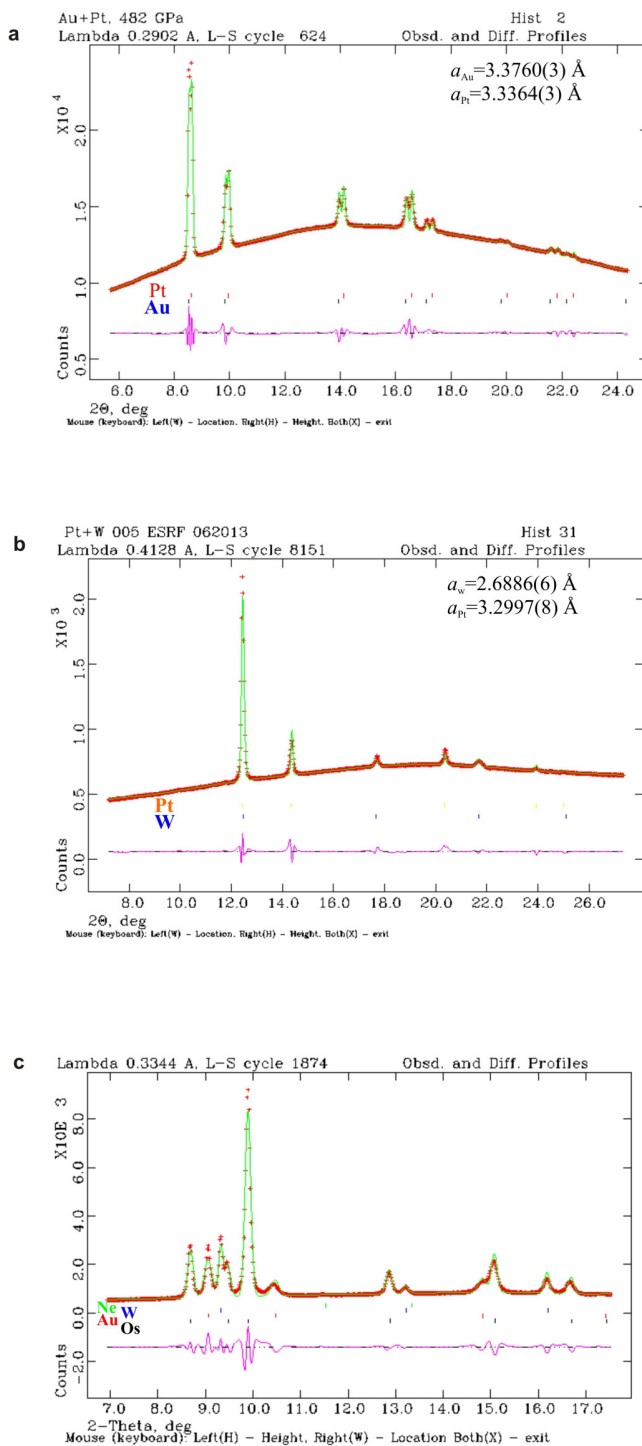
established in equation (4). Similar to the ETT, the anisotropy might be strengthened by a modification of the non-local pseudopotential, equations (1) and (2), acting on the valence electrons, owing to substantial reconstruction of inner $5p$ and $4f$ states at the transition. In the model given by equation (3), reconstruction of the inner states affects the electron–ion interaction via the ion core polarizability at imaginary frequencies. The derivation of equation (3) is based on the diagram consideration of the model of polarized ions in electron gas that is suggested in ref. 52. All the two-ion contributions to the total energy (that is, all diagrams containing two polarizability blocks) can be separated into two classes: one is the van der Waals interaction screened by itinerant electrons⁵²; the other, as was demonstrated in ref. 50, can be interpreted as a second-order contribution of the pseudopotential, equation (3), with the only assumption being that the energy of excitation of the ionic core is higher than typical energies of the itinerant-electron subsystem (such as plasma frequency and the Fermi energy). More details can be found in refs 27 and 53.

31. Georges, A., Kotliar, G., Krauth, W. & Rozenberg, M. J. Dynamical mean-field theory of strongly correlated fermion systems and the limit of infinite dimensions. *Rev. Mod. Phys.* **68**, 13–125 (1996).
32. Boehnke, L. *et al.* Orthogonal polynomial representation of imaginary-time Green's functions. *Phys. Rev. B* **84**, 075145 (2011).
33. Aichhorn, M. *et al.* Dynamical mean-field theory within an augmented plane-wave framework: assessing electronic correlations in the iron pnictide LaFeAsO. *Phys. Rev. B* **80**, 085101 (2009).
34. Aichhorn, M., Pourovskii, L. & Georges, A. Importance of electronic correlations for structural and magnetic properties of the iron pnictide superconductor LaFeAsO. *Phys. Rev. B* **84**, 054529 (2011).
35. Gull, E. *et al.* Continuous-time Monte Carlo methods for quantum impurity models. *Rev. Mod. Phys.* **83**, 349–404 (2011).
36. Beach, K. S. D. Identifying the maximum entropy method as a special limit of stochastic analytical continuation. Preprint at <http://arxiv.org/abs/cond-mat/0403055> (2004).
37. Solov'yev, I. V., Dederichs, P. H. & Anisimov, V. I. Corrected atomic limit in the local-density approximation and the electronic structure of d impurities in Rb. *Phys. Rev. B* **50**, 16861–16871 (1994).
38. Czyzyk, M. T. & Sawatzky, G. A. Local-density functional and on-site correlations: the electronic structure of La_2CuO_4 and LaCuO_3 . *Phys. Rev. B* **49**, 14211–14228 (1994).
39. Hohenberg, P. & Kohn, W. Inhomogeneous electron gas. *Phys. Rev.* **136**, B864–B871 (1964).
40. Blaha, P., Schwarz, K., Madsen, G., Kvasnicka, D. & Luitz, J. *WIEN2k, An Augmented Plane Wave + Local Orbitals Program for Calculating Crystal Properties* (Karlheinz Schwarz, Techn. Universität Wien, Austria, 2001).
41. Wills, J. M. *et al.* *Full-Potential Electronic Structure Method* (Springer, 2010).
42. Armiento, R. & Mattsson, A. E. Functional designed to include surface effects in self-consistent density functional theory. *Phys. Rev. B* **72**, 085108 (2005).
43. Mattsson, A. E. & Armiento, R. Implementing and testing the AM05 spin density functional. *Phys. Rev. B* **79**, 155101 (2009).
44. Perdew, J. P., Burke, K. & Ernzerhof, M. Generalized gradient approximation made simple. *Phys. Rev. Lett.* **77**, 3865–3868 (1996); erratum. **78**, 1396 (1997).
45. Haas, P., Tran, F. & Blaha, P. Calculation of the lattice constant of solids with semilocal functional. *Phys. Rev. B* **79**, 085104 (2009); erratum. **79**, 209902 (2009).
46. Ruban, A. V. & Abrikosov, I. A. Configurational thermodynamics of alloys from first-principles: effective cluster interactions. *Rep. Prog. Phys.* **71**, 046501 (2008).
47. Pourovskii, L. V. *et al.* Impact of electronic correlations on the equation of state and transport in ϵ -Fe. *Phys. Rev. B* **90**, 155120 (2014).
48. Katsnelson, M. I. & Trefilov, A. V. Fermi-liquid theory of electronic topological transitions and screening anomalies in metals. *Phys. Rev. B* **61**, 1643–1645 (2000).
49. Nizhankovskii, V. I. *et al.* Anisotropy of the thermal expansion of titanium due to proximity to an electronic topological transition. *JETP Lett.* **59**, 733–737 (1994).
50. Souvatzis, P., Eriksson, O. & Katsnelson, M. I. Anomalous thermal expansion in alpha-titanium. *Phys. Rev. Lett.* **99**, 015901 (2007).
51. Vaks, V. G. *et al.* Pre-transition softening and anomalous pressure dependence of shear constants in alkali and alkaline-earth metals due to band-structure effects. *J. Phys. Condens. Matter* **3**, 1409–1428 (1991).
52. Rehr, J. J., Zaremba, E. & Kohn, W. van der Waals forces in the noble metals. *Phys. Rev. B* **12**, 2062–2066 (1975).
53. Vonsovsky, S. V., Katsnelson, M. I. & Trefilov, A. V. Localized and itinerant behavior of electrons in metals. *Phys. Met. Metallogr.* **76**, 247–299 (1993).
54. Dewaele, A., Loubeire, P. & Mezouar, M. Equations of state of six metals above 94 GPa. *Phys. Rev. B* **70**, 094112 (2004).
55. Litasov, K. D. *et al.* Thermal equation of state to 33.5 GPa and 1673 K and thermodynamic properties of tungsten. *J. Appl. Phys.* **113**, 133505 (2013).
56. Sahu, B. R. & Kleinman, L. Osmium is not harder than diamond. *Phys. Rev. B* **72**, 113106 (2005).
57. Dorfman, S. M., Prakapenka, V. B., Meng, Y. & Duffy, T. S. Intercomparison of pressure standards (Au, Pt, Mo, MgO, NaCl and Ne) to 2.5 Mbar. *J. Geophys. Res.* **117**, B08210 (2012); errata **117**, B11204 (2012).
58. Fei, Y. *et al.* Toward an internally consistent pressure scale. *Proc. Natl Acad. Sci. USA* **104**, 9182–9186 (2007).

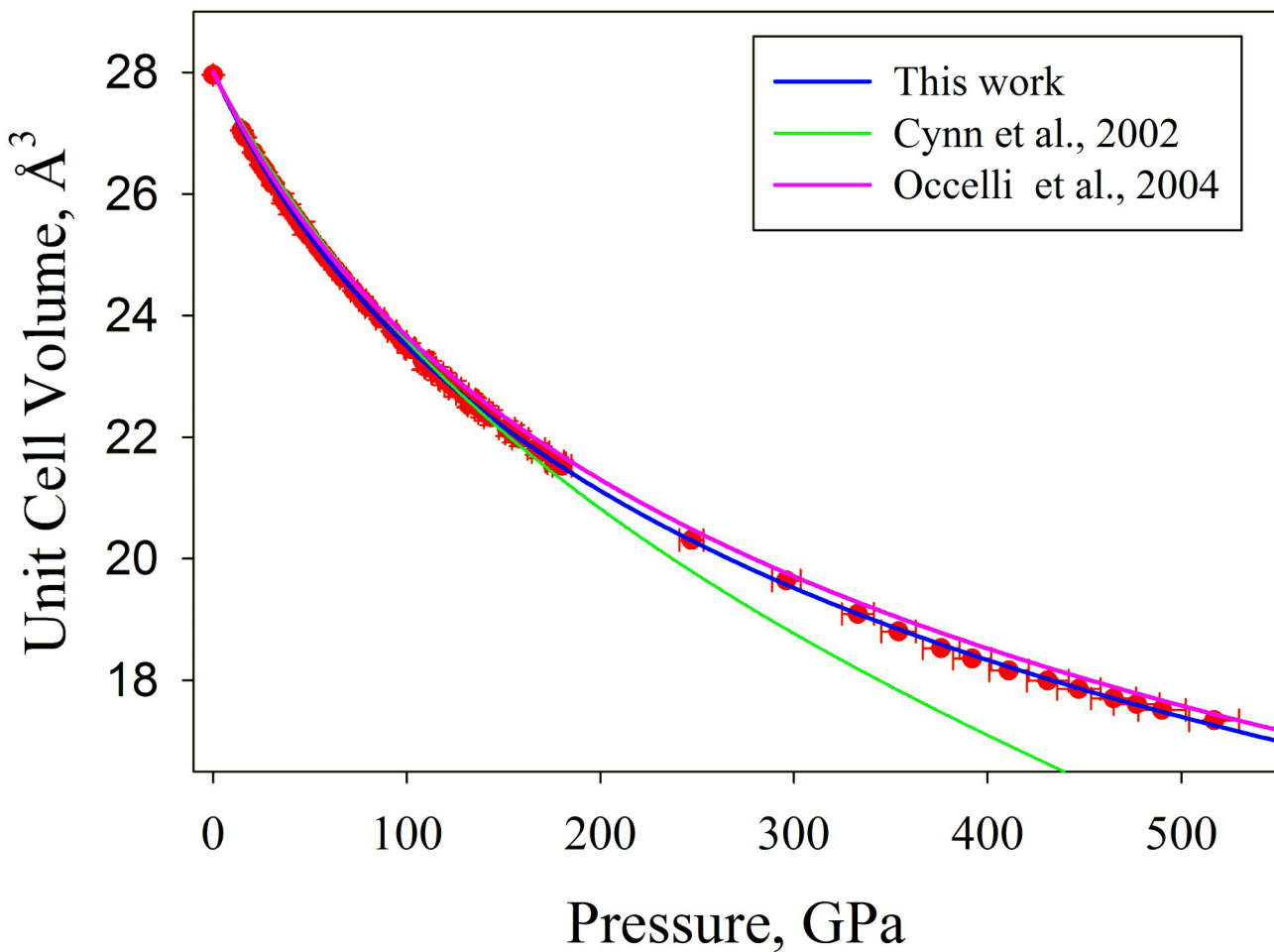


Extended Data Figure 1 | Equations of state of W. **a**, Comparison of different EOSs of W reported in Dewaele *et al.*⁵⁴, Sokolova *et al.*²³, and Litasov *et al.*⁵⁵, and this work. Although the curves agree for pressures up to about 50 GPa, there is a substantial discrepancy for pressures around 0.5 TPa. **b**, Pressure dependence of the unit cell volume of W. Experimental data points (red solid

dots represent data collected using a Au–W mixture, green diamonds using a Pt–W mixture) were fitted using the third-order Birch–Murnaghan EOS (blue solid line, $V_0 = 31.674(3)$ Å³ per unit cell, $K_{300} = 307(2)$ GPa, $K' = 4.53(4)$); data are equally well fitted with the Vinet EOS ($V_0 = 31.686(7)$ Å³ per unit cell, $K_{300} = 302(1)$ GPa, $K' = 4.82(3)$).

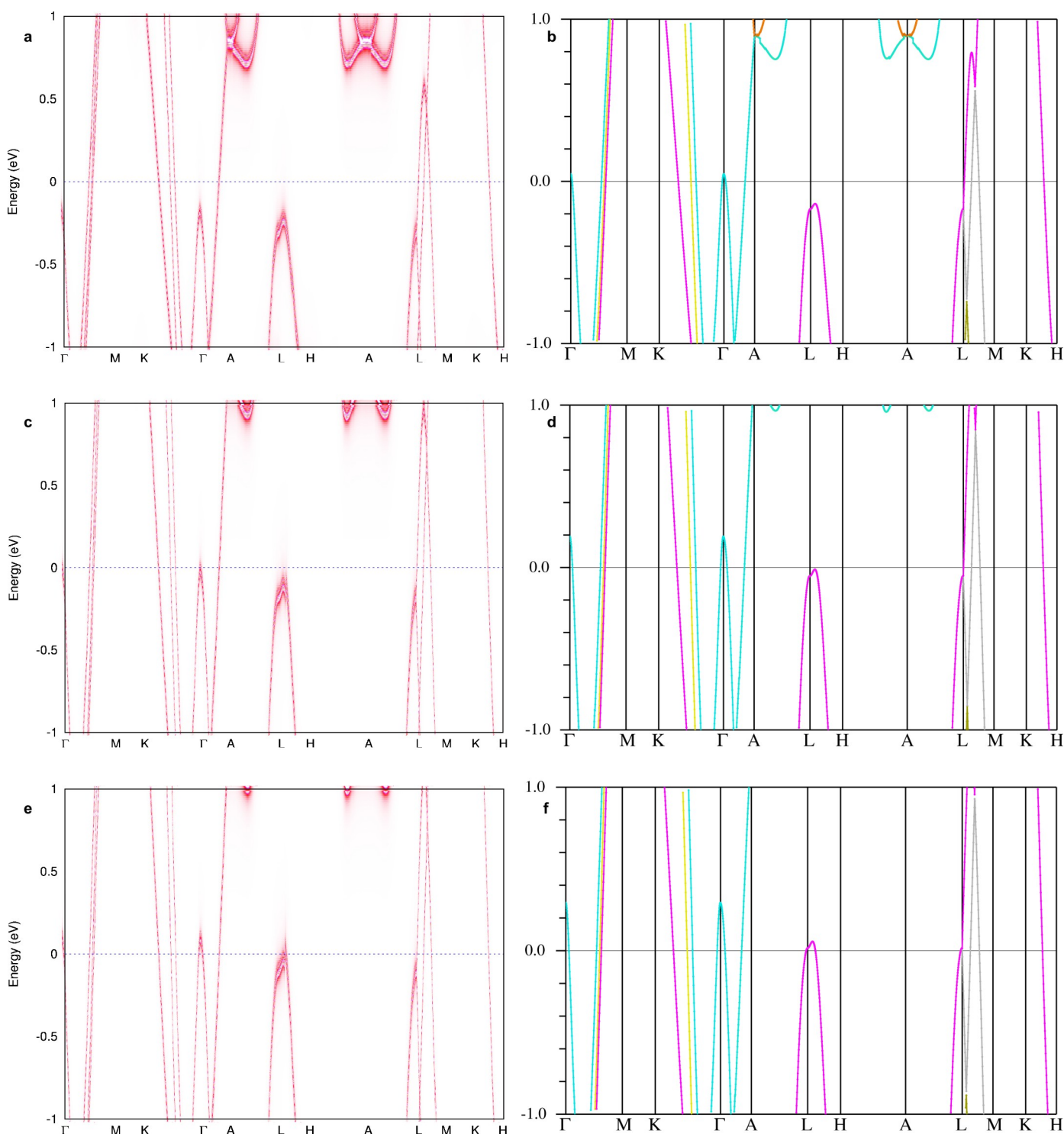


Extended Data Figure 2 | Examples of the full-profile (GSAS) treated diffraction patterns. **a**, Au–Pt mixture collected in a dsDAC at 482(5) GPa (Au pressure scale from ref. 20). Even at pressures in the proximity of 5 Mbar, powder X-ray diffraction data are sufficient to clearly resolve peaks of Au and Pt, and accurately determine lattice parameters of both metals. **b**, W–Pt mixture, unsuccessful experiment in a dsDAC. According to the W EOS, the pressure is 461(7) GPa, whereas according to the Pt EOS, it is 559(10) GPa. This inconsistency in pressures is a result of an inhomogeneous distribution of the two metals between secondary anvils in the dsDAC; such data cannot be used for constraining EOSs. This observation also shows that very large pressure gradients are possible in dsDACs. **c**, Mixture of Os ($a = 2.5404(6) \text{ Å}$, $c = 4.0386(10) \text{ Å}$), W ($a = 2.9133(5) \text{ Å}$), and Au ($a = 3.6657(6) \text{ Å}$) collected in a conventional DAC (Ne used as the pressure transmitting medium) at a pressure of 134(2) GPa.



Extended Data Figure 3 | Experimental dependence of the unit cell volume of Os on pressure in comparison with EOSs reported in the literature. The magenta line is from Occelli *et al.*³ ($K_{300} = 421 \text{ GPa}$, $K' = 4.0$) and the green line is from Cynn *et al.*⁴ ($K_{300} = 463 \text{ GPa}$, $K' = 2.8$). These

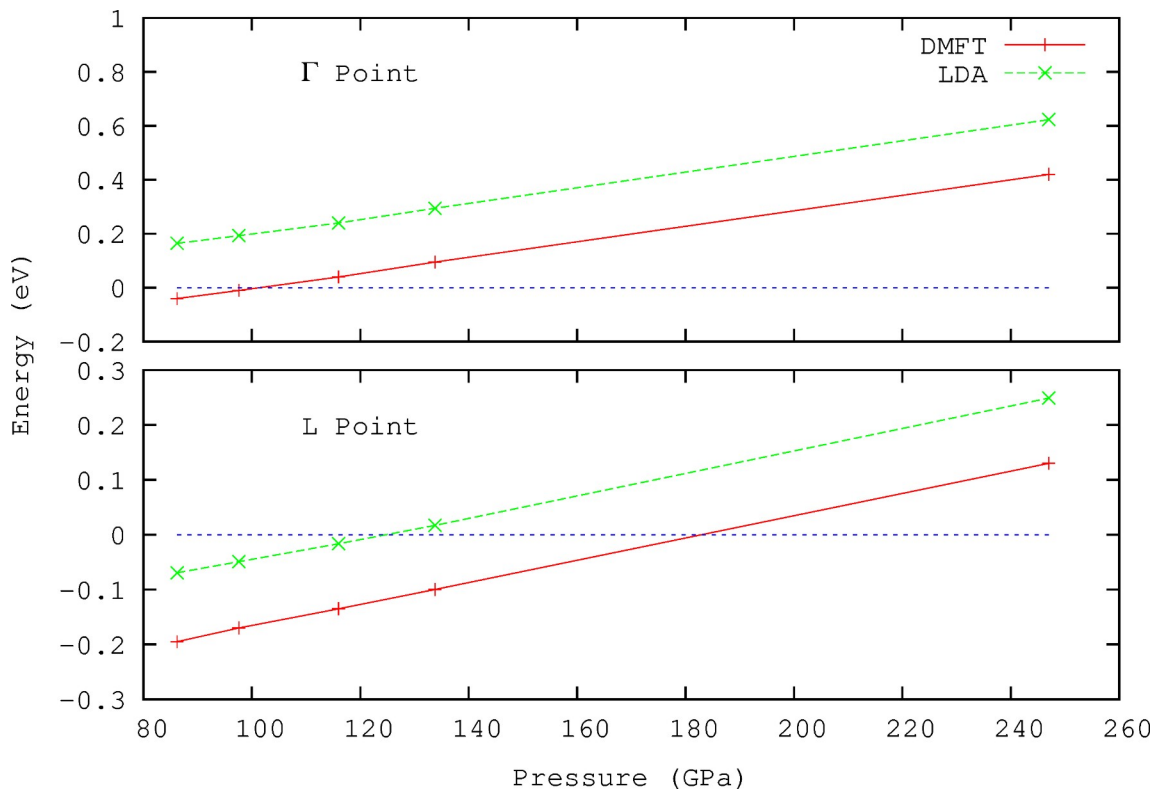
data have been re-fitted using the ruby pressure scale as suggested in refs 20, 22 and references therein. Experimental data points (solid red dots) were fitted using the third-order Birch-Murnaghan EOS (blue line, $V_0 = 28.02(4) \text{ \AA}^3$ per unit cell, $K_{300} = 399(6) \text{ GPa}$, $K' = 4.04(4)$).



Extended Data Figure 4 | Electronic band structure of Os at moderate compressions along the high-symmetry lines in the hcp Brillouin zone.

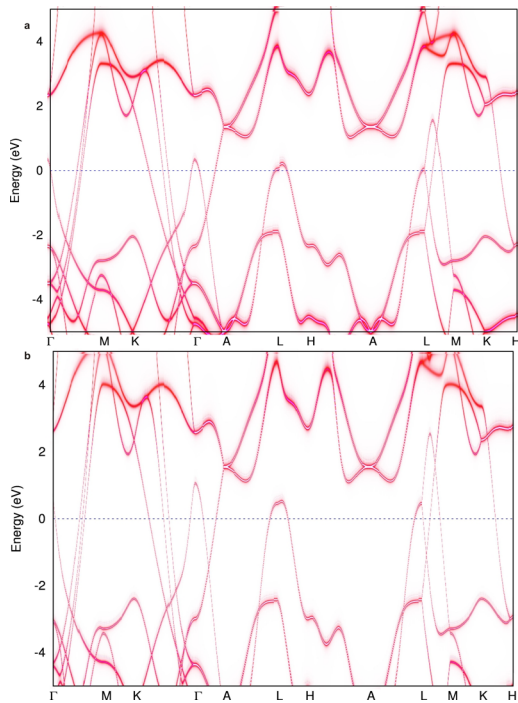
Energies are given relative to the Fermi energy, which is taken to be zero. Calculations are carried out at pressures of 0 GPa (a, b), 97.5 GPa (c, d), and 134 GPa (e, f). a, c, e, The k -resolved spectral functions $A(k, \omega)$ obtained with LDA+DMFT. b, d, f, The band structure obtained with LDA. In both cases, we used the experimental lattice parameters ($a = 2.734 \text{ \AA}$, $c/a = 1.580$ at 0 GPa; $a = 2.578 \text{ \AA}$, $c/a = 1.589$ at 97.5 GPa; $a = 2.540 \text{ \AA}$, $c/a = 1.590$ at

134 GPa). Our LDA+DMFT calculations predict that two ETTs occur in hcp Os upon compression. In a, a band at the Γ point is well below the Fermi energy at ambient pressure; however, it nearly touches the Fermi energy at 97.5 GPa, and the corresponding hole pocket has already appeared at 134 GPa, giving rise to a change of the Fermi surface topology, that is, to an electronic topological transition at about 101.5 GPa (Extended Data Fig. 5). Our LDA+DMFT calculations also indicate that another ETT at the L point should occur above 134 GPa, at about 183 GPa (Extended Data Fig. 5).



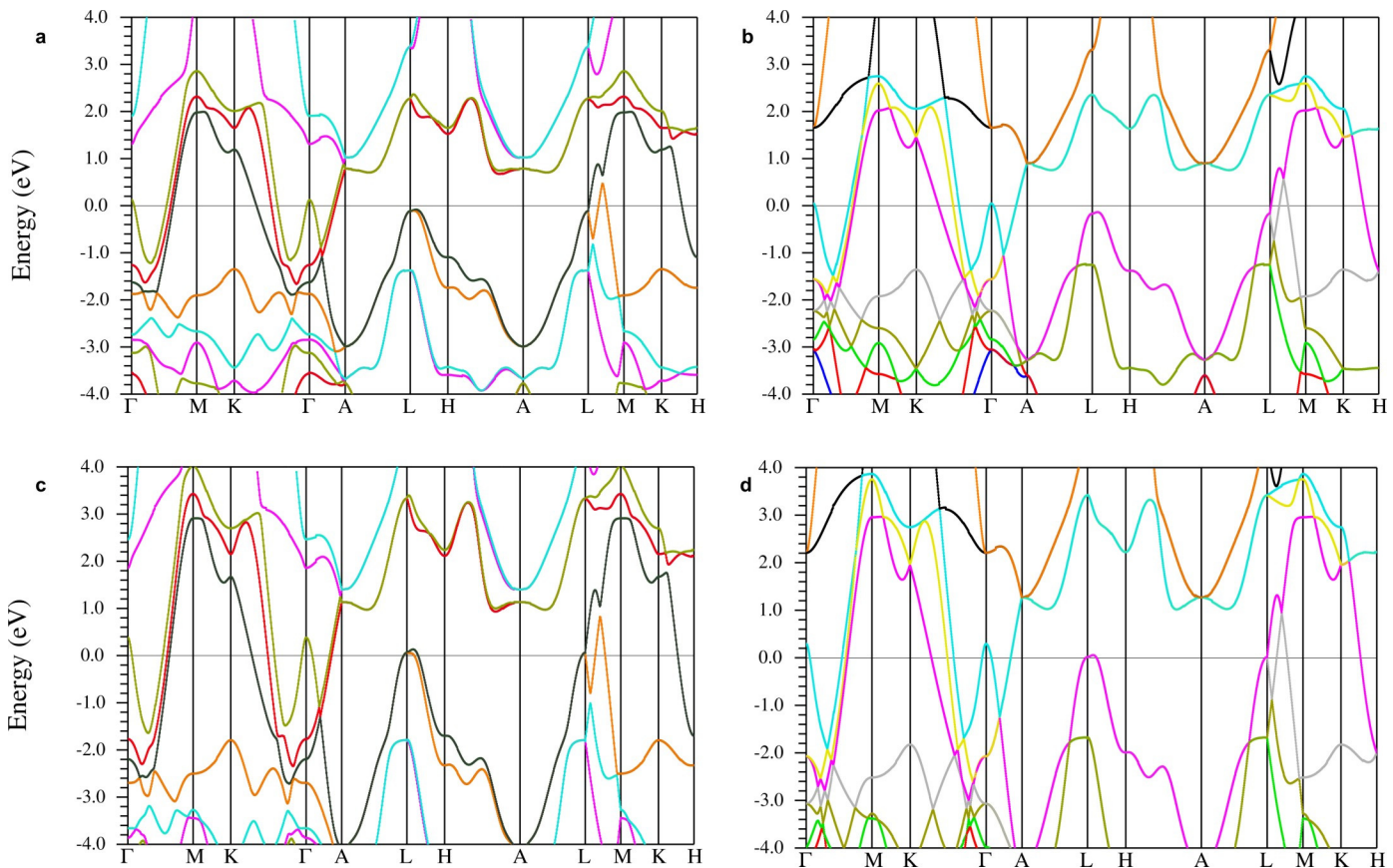
Extended Data Figure 5 | The position of the relevant bands at the Γ (top) and L (bottom) points obtained from LDA+DMFT and LDA calculations as a function of pressure. The positive values indicate appearance of the corresponding hole pockets. Energies are given relative to the Fermi energy. A closer examination of the band shape in the vicinity of the L point reveals that this hole pocket first appears along the L-H line and then extends to include

the L point. To estimate more precisely the critical pressures for the ETTs, we plot the positions of the relevant bands at the Γ and L points with respect to the Fermi level and obtain the values of the critical pressures by interpolation. The LDA+DMFT calculations predict that the hole pockets at the Γ and L points appear at about 101.5 GPa and 183 GPa, respectively.



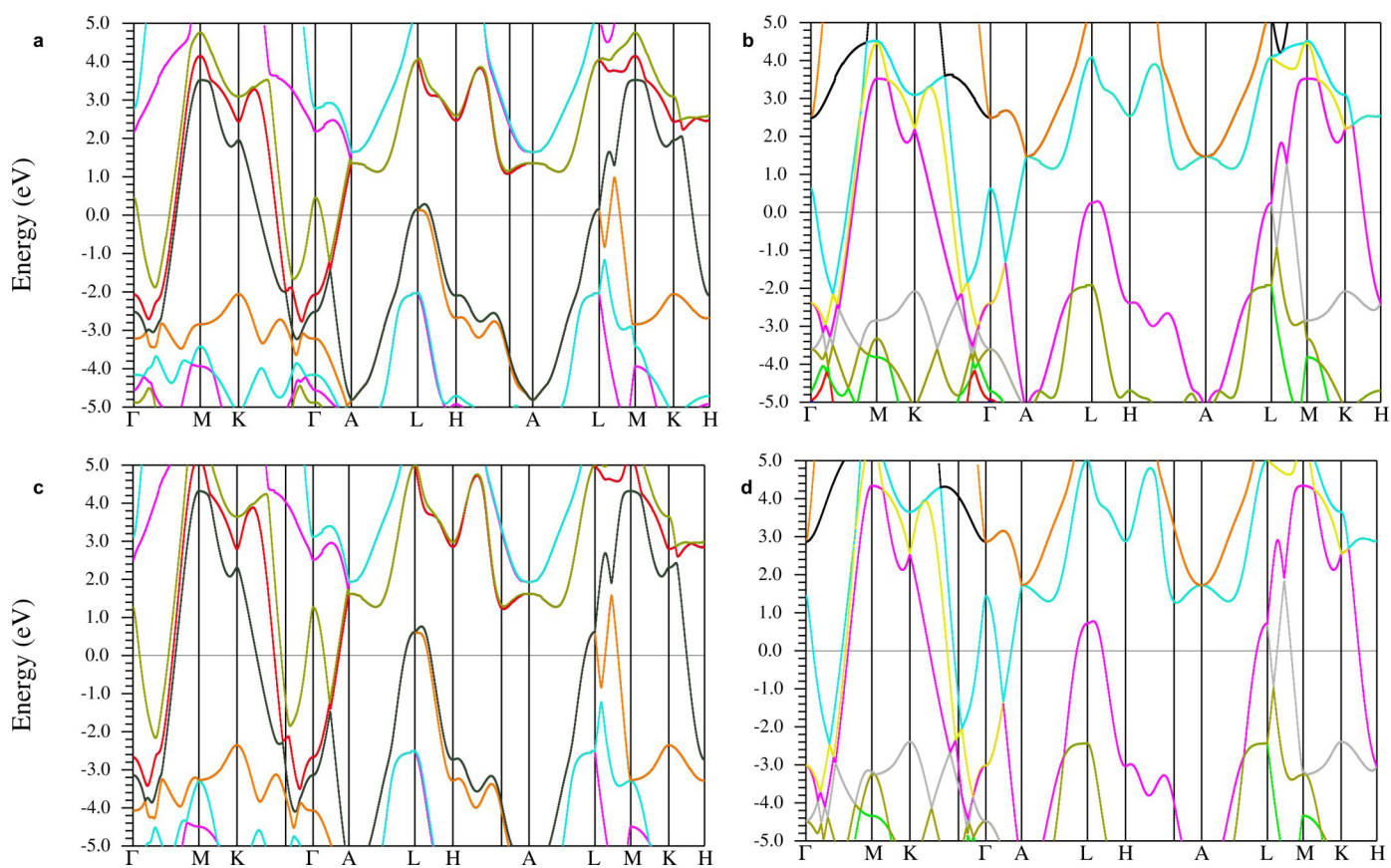
Extended Data Figure 6 | k -resolved spectral functions $A(k, \omega)$ of Os at ultra-high compressions along the high-symmetry lines in the hcp

Brillouin zone. **a, b,** Calculations are carried out at pressures of 247 GPa (a) and 477 GPa (b) using LDA+DMFT. The experimental lattice parameters were used in the calculations ($a = 2.449 \text{ \AA}$, $c/a = 1.596$ at 247 GPa; $a = 2.335 \text{ \AA}$, $c/a = 1.597$ at 477 GPa). Energies are given relative to the Fermi energy, which is taken to be zero. Hole pockets are present at the Γ and L points at $P = 247 \text{ GPa}$. Increasing the pressure to 477 GPa does not induce any new ETTs. Moreover, no features of the band structure suggest that new ETTs might be induced by further increase of the pressure within reasonable limits.



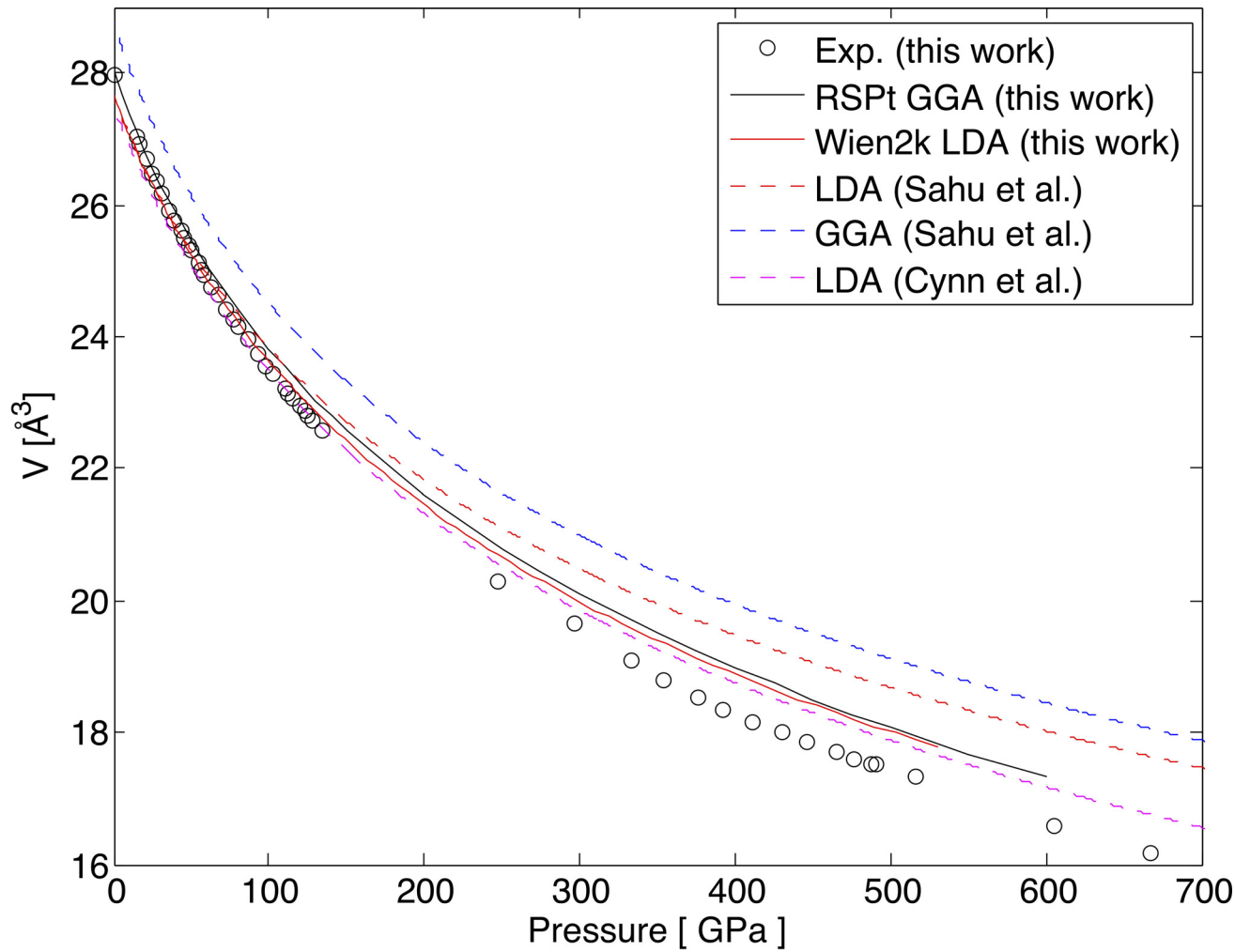
Extended Data Figure 7 | Electronic band structure of Os at moderate compressions along the high-symmetry lines in the hcp Brillouin zone.
a–d, Band structure of Os at 0 GPa (**a**, **b**) and at 134 GPa (**c**, **d**). Energies are given relative to the Fermi energy. In **a** and **c**, spin-orbit coupling has been

included, whereas in **b** and **d**, the energies were obtained with the scalar-relativistic approximation. Experimental lattice parameters were used in the calculations (see Extended Data Fig. 4). Bands are shown in different colours for clarity.



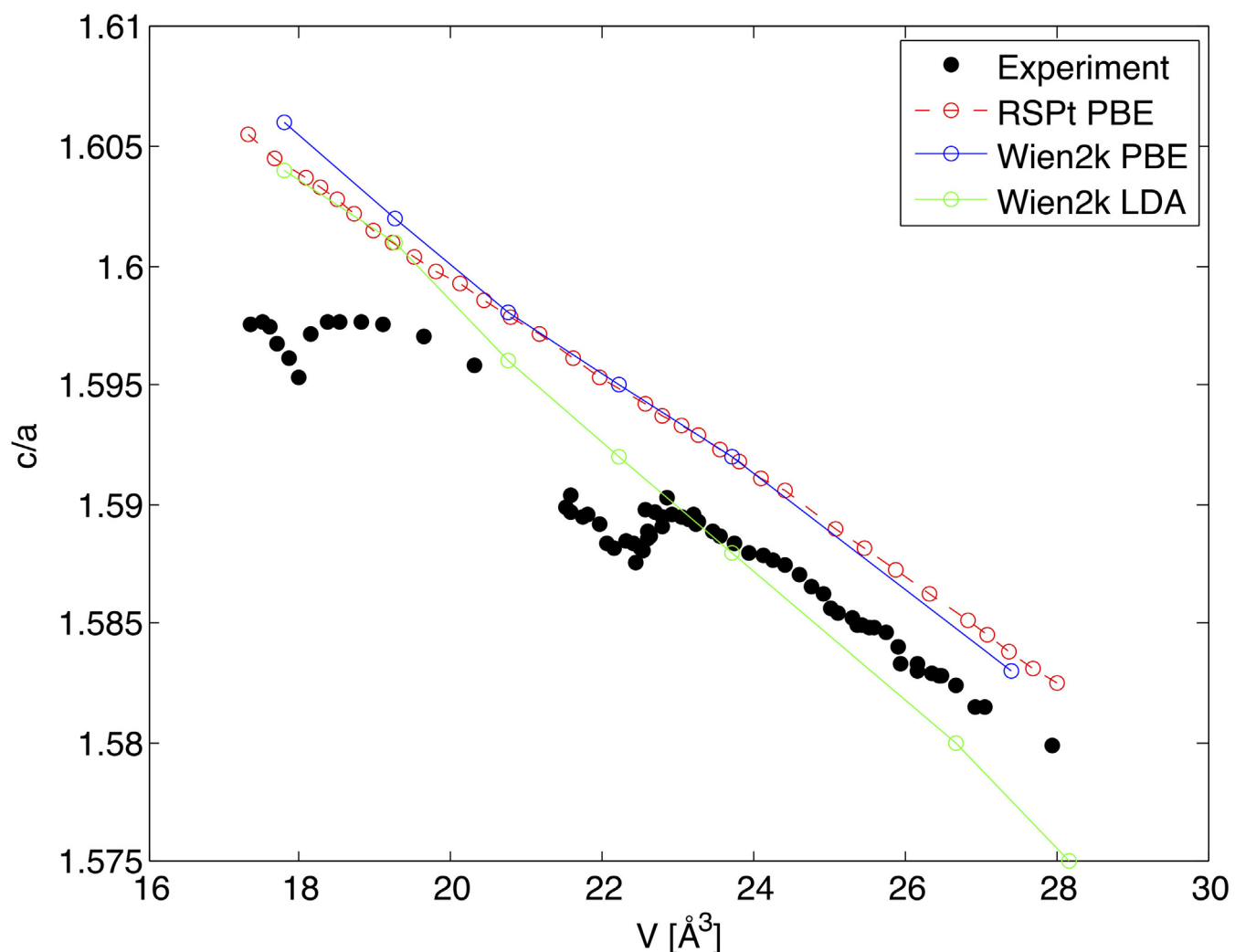
Extended Data Figure 8 | Electronic band structure of Os at extreme compressions along the high-symmetry lines in the hcp Brillouin zone.
a–d, Band structure of Os at 247 GPa (**a, b**) and at 477 GPa (**c, d**). Energies are given relative to the Fermi energy. In **a** and **c**, spin-orbit coupling has been

included, whereas in **b** and **d**, the energies were obtained with the scalar-relativistic approximation. Experimental lattice parameters were used in the calculations (see Extended Data Fig. 6).



Extended Data Figure 9 | Comparison of the EOS for hcp Os calculated using different approximations within DFT with the experimental EOS measured in this work. Shown are GGA calculations carried out by us using the RSPT method (black solid line) and by Sahu *et al.*⁵⁶ (blue dashed line), as well as LDA calculations carried out by us using the Wien2k method (red solid line), by Cynn *et al.*⁴ (pink dashed line), and by Sahu *et al.*⁵⁶ (red dashed line). The experimental EOS obtained in this work is shown with black circles. The different curves agree reasonably well for pressures up to about 50 GPa. In contrast, there is noticeable discrepancy at ultra-high pressure, and there is no theoretical EOS that accurately describes the experiment for pressures around 0.5 TPa. Local and semi-local approximations within DFT are insufficient to describe the P - V relationship of Os under extreme conditions. Part of the reason for the disagreement between theory and experiment might be related to the improper account of the many-electron effects within the theory. In principle, LDA and GGA work better at high pressure; however, errors that might be important at low pressure⁴⁷ could propagate through the EOS to the whole pressure range, owing to the use of all the calculated points in the fitting of the energy versus volume data by, for example, the third-order Birch-Murnaghan EOS used in this work. To justify this statement, consider the calculated EOS parameters, summarized in Extended Data Table 1. The

equilibrium volumes calculated by us differ from the experiment (Extended Data Table 1) by less than 1.5%. On the other hand, the overestimation of the calculated bulk moduli (B) and their pressure derivatives (B') is greater, about 10%. Our EOS parameters are within the range of theoretical parameters available in the literature, which are fitted for $P < 100$ GPa (Extended Data Table 1). We deal with a highly incompressible metal, for which typical DFT errors in B , and especially in B' , translate into large differences in P - V relationships at ultra-high pressure. Even in this regime, the error in volume at a fixed pressure remains within typical DFT limits of about 2%–3%. However, the pressure calculated at fixed volume can differ by several tens of gigapascals. This difference is due to errors in B and B' calculated at ambient pressure, coupled to a very high value of B . The use of more advanced theoretical methods could improve the calculated EOS. In ref. 47, a substantial reduction of B in isoelectronic hcp Fe is demonstrated using a LDA+DMFT approach. Here the effect is expected to be smaller, but may still be sufficient to improve the agreement with experiment. Our results demonstrate a need to further develop the electronic structure theory, with the experiment reported here providing a bench-mark for the theory. On the other hand, we consistently used experimental lattice parameters in the discussion of the electronic structure of Os in this study.



Extended Data Figure 10 | Comparison of the ratio of the lattice parameters c/a for hcp Os. The ratio is calculated using the RSPT method at $T = 0$ K with a PBE-GGA (red dashed line), and using Wien2k with a LDA (green line) and a PBE-GGA (blue line). The room-temperature experimental results obtained in this work are shown with filled black dots. Agreement between the calculated and experimental c/a ratio is typical for DFT calculations. The theoretical results do not show any peculiarity of the lattice-parameter ratio;

however, the calculations are carried out at $T = 0$ K, whereas the experimental data are taken at room temperature. Therefore, a direct comparison between theory and experiment is nontrivial (Methods). In hcp metals, the effect of the electronic transitions on the lattice-parameter ratio should become visible at finite temperatures, owing to the peculiarities of the thermal expansion coefficients, which are anisotropic along different directions of the crystal lattice.

Extended Data Table 1 | EOS parameters of Au, Pt, W, and Os

a	Metal	3 rd order Birch–Murnaghan EOS			Vinet EOS			Reference; Range
		V ₀ , Å ³ /unit cell	K ₃₀₀ , GPa	K'	V ₀ , Å ³ /unit cell	K ₃₀₀ , GPa	K'	
	Au	67.85	167.5	5.61	67.85	167	5.88	20:550GPa
					67.85	167	6.0	57:250 GPa
	Pt	60.389(5)	274(2)	5.23(3)	60.381(5)	261(2)	5.83(3)	58:100 GPa This work 480 GPa
		60.38	276.4	5.12	60.38	277	5.08	20:550GPa 54:94 GPa
					60.38	277	5.43	57:250 GPa
	W	31.674(3)	306.8(1.5)	4.53(4)	31.686(7)	301.9(1.2)	4.82(3)	200 GPa This work 517 GPa
					31.724	296	4.30	54:94 GPa
					31.691	317	3.16	55:33 GPa
					31.72	308	4.25	23:400 GPa
	Os	28.02(4)	398.5(5.9)	4.04(4)	28.08(5)	380(7)	4.48(6)	4:65 GPa 3:75 GPa 2:58 GPa
		27.96	462	2.4				
		27.941	411	4.0				
		27.977	395	4.5				

b		V [Å ³]	B [GPa]	B'
	GGA (RSPT, this work)	28.00	448	4.29
	GGA (RSPT, this work, fitted at P<100 GPa)	28.00	423	4.67
	GGA (Ref. 56)	28.72	401	5.47
	GGA (Ref. 3)		382	4.60
	LDA (Wien2k, this work)	27.66	447	4.41
	LDA (Ref. 3)		437	4.46
	LDA (Ref. 56)	27.60	454	5.26
	LDA (Ref. 4)	27.50	445	4.4

a, Experimental data; b, theoretical data. Values in a are from this work and refs 2–4, 20, 23, 54, 55, 57, and 58. Presented in b are GGA calculations carried out by us using the RSPT method and the calculations presented in ref. 56, as well as LDA calculations carried out by us using the Wien2k method and the calculations presented in refs 3, 4, and 56.